Computers & Fluids 71 (2013) 417–425

Contents lists available at SciVerse ScienceDirect

Computers & Fluids

journal homepage: www.elsevier.com/locate/compfluid

Image-based fluid–structure interaction model of the human mitral valve

Xingshuang Ma [a], Hao Gao [a], Boyce E. Griffith [b], Colin Berry [c], Xiaoyu Luo [a,*]

[a] School of Mathematics and Statistics, University of Glasgow, University Gardens, Glasgow G12 8QW, UK
[b] Leon H. Charney Division of Cardiology, Department of Medicine, New York University School of Medicine, 550 First Avenue, New York, NY 10016, USA
[c] Institute of Cardiovascular and Medical Sciences, University of Glasgow, Glasgow G12 8QW, UK

ARTICLE INFO

Article history:
Received 3 July 2012
Received in revised form 12 September 2012
Accepted 31 October 2012
Available online 15 November 2012

Keywords:
Human mitral valve
Clinical imaging
Magnetic resonance imaging
Fluid–structure interaction
Immersed boundary method

ABSTRACT

The mitral valve (MV) is one of the four cardiac valves. It consists of two leaflets that are connected to the left ventricular papillary muscles via multiple fibrous chordae tendinae. The primary functions of the MV are to allow for the free flow of blood into the left ventricle (LV) of the heart from the left atrium (LA) during the diastolic and early systolic phases of the cardiac cycle, and to prevent regurgitant flow from the LV to the LA in deep systole. MV disorders such as mitral stenosis and regurgitation cause significant morbidity and mortality, and an improved understanding of MV biomechanics could lead to improved medical and surgical procedures to restore normal MV function in patients with such disorders. Computational models can realistically capture the anatomical and functional features of the MV and hence can provide detailed spatial and temporal data that may not be easily obtained clinically or experimentally. In this study, an anatomical model of a human MV is derived from in vivo magnetic resonance imaging (MRI) data. Using this clinical imaging-derived model, fluid–structure interaction (FSI) simulations are performed using the immersed boundary (IB) method under physiological, dynamic transvalvular pressure loads. Computational analyses show that the subject-specific MV geometry has a significant influence on the simulation results. An initial validation of the model is achieved by comparing the opening height and flow rates to clinical measurements.

1. Introduction

Cardiovascular disease is the leading cause of mortality in industrialised nations, including the United Kingdom and the United States. In 2007, cardiovascular disease accounted for 34% of deaths in the UK, totalling just over 193,000 people. When cardiac valve function is sufficiently impaired, valve repair or replacement is required. Approximately 39,000 patients have cardiac surgery in the UK annually, among which heart valve operations are the second most common, behind only coronary bypass procedures.

The mitral valve (MV) is a complex apparatus consisting of two leaflets, a large antero-medial leaflet and a smaller postero-lateral leaflet, that are each connected via multiple fibrous chordae tendinae to papillary muscles that attach to the wall of the left ventricle (LV) of the heart. The MV opens to allow blood to fill the LV during diastole and early systole, and MV closure regulates and prevents systolic regurgitation of blood from the LV into the left atrium (LA). This function requires the coordinated action of these interrelated elements, and alterations in the structure or function of the leaflets, chordae, or papillary muscles may impede left ventricular filling, induce mitral regurgitation, and alter left ventricular ejection [1]. An improved understanding of human mitral valve biomechanics is urgent and important for the optimisation of medical therapies and surgical procedures aimed at restoring normal MV function in patients with valvular heart diseases.

Comprehensive assessment of MV physiology and pathophysiology requires detailed modelling of patient anatomy and dynamics, and for such assessments to be clinically useful, they must be based on noninvasive imaging data. Dynamic modelling of MV biomechanics is made challenging by the large deformations experienced by the leaflets, the anisotropic nonlinear elastic behaviour of the valvular tissue, and the pulsatile haemodynamic loads during the cardiac cycle. In addition, there is large inter-subject variability in the anatomy of the MV apparatus. Imaging techniques such as magnetic resonance (MR) imaging and echocardiography [2] allow the visualisation of the cardiac valves and provide data needed to link anatomy to valvular function, but such imaging modalities do not yield information on the loads applied to the valve that arise from the coupled fluid and structural dynamics of the valve and the blood [3]. Numerical simulation has the potential to provide detailed biomechanical data, such as in vivo loads and tissue stresses, that may not be easily determined by standard clinical or experimental techniques. Therefore, imaging-derived computational models that account for the observed physiological conditions are an avenue to further quantitative and qualitative insight into valvular function. Such data could be used to develop

* Corresponding author.
E-mail address: xiaoyu.luo@glasgow.ac.uk (X.Y. Luo).

0045-7930/$ - see front matter © 2012 Elsevier Ltd. All rights reserved.
http://dx.doi.org/10.1016/j.compfluid.2012.10.025

quantitative methods for determining patient-specific medical and surgical strategies for the treatment of valvular heart diseases.

Computational studies of the MV have been performed by a number of groups, many of whom have used structural modelling to study MV biomechanics. Prot and co-workers reported their work on MV simulations in a series of studies using a transversely isotropic strain–energy functional using the nonlinear finite element code ABAQUS [4–8]. The effect of annular dilation and correction have both been studied by Votta et al. [9,10]. Three-dimensional dynamic modelling of the ovine MV has also been performed by Lim et al. [11], who focused on the asymmetric stress pattern of the MV. Purely structural heart valve models appear to be primarily suitable for simulating static configurations, such as fully-opened or closed valves. Because of the strong interaction between the blood flow with the MV leaflets and the left ventricular wall, models of the full dynamic behaviour of the MV require the description of fluid–structure interaction (FSI) [3]. Kunzelman, Einstein, and co-workers were the first to use a three-dimensional fluid-coupled computational model to simulate normal mitral function [12–14]; the biomechanics underlying valvular disease [15,16]; and surgical interventions [16,17]. A limitation of most of these studies is that the valve geometries have typically been taken to be symmetric about the mid-line of the anterior and posterior leaflets [11]; however, the MV is a fully three-dimensional structure.

Our group has previously developed a sequence of fully three-dimensional FSI models of a prosthetic MV [18–22]. In these studies, the dynamic behaviour of a chorded polyurethane mitral prosthesis was modelled using the immersed boundary (IB) method, which accounts for the fluid–structure interaction between the blood flow and the MV leaflets. Unlike the native valve, this prosthesis is actually symmetric about the mid-lines of the leaflets, and this symmetry was accounted for in the model. In some of these studies, the motion of the LV was determined by high-resolution MR imaging of a normal human ventricle, which was used as a downstream boundary condition [21]. We also demonstrated the effects of incorporating a model of the bending rigidity of the valve leaflets [22], which is needed to obtain accurate flow rates and open configurations, despite the fact that MV leaflets are extremely thin structures.

In this paper, we describe dynamic modelling of the human MV that uses patient-specific anatomy derived from MR imaging data along with physiological, semi-subject-specific loading conditions. Echocardiography has been historically preferred in the literature for cardiac diagnostic applications [2] because it offers good temporal resolution, is safe, and is relatively inexpensive. However, it is difficult to reconstruct the geometry of the MV leaflets from echocardiographic images. By contrast, MR imaging provides much higher image quality, primarily because of the higher spatial resolution offered by MR imaging and its lack of speckle texture, and simplifies the determination of subject- and patient-specific anatomy. In our simulations, the image-derived MV model is mounted in a semi-rigid tube, and dynamic boundary conditions are imposed at the inlet and outlet of this tube to produce physiological transvalvular pressure differences. The equations of fluid–structure interaction are solved using a staggered-grid version [23–25] of a formally second-order accurate IB method [26,27]. This discretization approach has been demonstrated to yield significantly improved volume conservation when compared to collocated versions of the IB method [24]. We use families of elastic fibres that resist extension, compression, and bending to model the thin MV leaflets and the chordae tendinae using measured human MV material properties [11,12,28–31]. We use a physiological driving pressure waveform [32] to simulate a complete cardiac cycle. To our knowledge, these are the first simulations of the human MV that use realistic, subject-specific valve geometry in the context of fluid–structure interaction and dynamic opening and closing with realistic transvalvular pressure loads.

2. The immersed boundary method

2.1. Mathematical formulation

The immersed boundary method for fluid–structure interaction treats problems in which an elastic structure is immersed in a viscous incompressible fluid. The immersed boundary formulation of such problems uses a Lagrangian description of the deformation and elasticity of the immersed structure along with an Eulerian description of the viscous incompressible fluid, which is modelled by incompressible Navier–Stokes equations. Interaction equations that take the form of integral equations with Dirac delta function kernels couple the Lagrangian and Eulerian frames. In the present work, we assume that the fluid possesses a uniform mass density ρ and dynamic viscosity μ, and that the immersed elastic structure is neutrally buoyant. We remark that although blood is non-Newtonian, a Newtonian description is generally considered to be adequate for flows in the heart and large vessels like those considered herein.

Let $\mathbf{x} = (x,y,z) \in \Omega$ denote Cartesian physical coordinates, in which $\Omega \in \mathbb{R}^3$ is the physical domain; let $\mathbf{s} = (r,s) \in U$ denote Lagrangian material coordinates attached to the structure, in which $U \in \mathbb{R}^2$ is the Lagrangian curvilinear coordinate domain; and let $\mathbf{X}(\mathbf{s},t) \in \Omega$ denote the physical position of material point $\mathbf{s}$ at time t. Throughout the present work, Ω is taken to be a rectangular box, so that $\Omega = [0,L_x] \times [0,L_y] \times [0,L_z]$. The equations of motion for the coupled fluid–structure system are

$$\rho\left(\frac{\partial \mathbf{u}}{\partial t}(\mathbf{x},t) + \mathbf{u}(\mathbf{x},t)\cdot\nabla\mathbf{u}(\mathbf{x},t)\right) = -\nabla p(\mathbf{x},t) + \mu\nabla^2\mathbf{u}(\mathbf{x},t) + \mathbf{f}(\mathbf{x},t), \quad (1)$$

$$\nabla\cdot\mathbf{u}(\mathbf{x},t) = 0, \quad (2)$$

$$\mathbf{f}(\mathbf{x},t) = \int_U \mathbf{F}(\mathbf{s},t)\,\delta(\mathbf{x}-\mathbf{X}(\mathbf{s},t))\,d\mathbf{s}, \quad (3)$$

$$\frac{\partial \mathbf{X}}{\partial t}(\mathbf{s},t) = \int_\Omega \mathbf{u}(\mathbf{x},t)\,\delta(\mathbf{x}-\mathbf{X}(\mathbf{s},t))\,d\mathbf{x}, \quad (4)$$

$$\mathbf{F}(\cdot,t) = \mathcal{F}[\mathbf{X}(\cdot,t)]. \quad (5)$$

Eqs. (1) and (2) are the incompressible Navier–Stokes equations, which are written in terms of the Eulerian velocity field $\mathbf{u}(\mathbf{x},t) = (u(\mathbf{x},t), v(\mathbf{x},t), w(\mathbf{x},t))$ and the Eulerian pressure field $p(\mathbf{x},t)$, along with a body force $\mathbf{f}(\mathbf{x},t)$ that is the Eulerian elastic force density applied by the structure to the fluid. Eq. (5) indicates that the Lagrangian elastic force density generated by the elasticity of the structure is determined by a time-independent functional of the configuration of the immersed structure; this functional is discussed below. Eqs. (3) and (4) are Lagrangian–Eulerian interaction equations that use integral transformations with three-dimensional Dirac delta function kernels, $\delta(\mathbf{x}) = \delta(x)\,\delta(y)\,\delta(z)$, to couple the Lagrangian and Eulerian descriptions. Specifically, Eq. (3) converts the Lagrangian elastic force density $\mathbf{F}$ into the equivalent Eulerian elastic force density $\mathbf{f}$. Notice that $\mathbf{F}$ and $\mathbf{f}$ have totally different characters: $\mathbf{F}(\mathbf{s},t)$ is a force density with respect to the curvilinear coordinate system (i.e. $\mathbf{F}(\mathbf{s},t)\,dr\,ds$ has units of force), whereas $\mathbf{f}(\mathbf{x},t)$ is a force density with respect to the physical coordinate system (i.e. $\mathbf{f}(\mathbf{x},t)\,dx\,dy\,dz$ has units of force). Nonetheless, $\mathbf{F}$ and $\mathbf{f}$ are equivalent as densities [33]. Eq. (4) states that the structure moves at the local fluid velocity, i.e.

$$\frac{\partial \mathbf{X}}{\partial t}(\mathbf{s},t) = \mathbf{u}(\mathbf{X}(\mathbf{s},t),t), \quad (6)$$

which is the no-slip condition of a viscous fluid.

2.2. Elasticity modelling

As in our earlier studies using the IB method to simulate the dynamics of cardiac valves [18–22], herein we treat the flexible leaflets of the MV as thin elastic boundaries and the chordae tendinae as elastic beams immersed in the fluid. The elasticity of these immersed structures is described by systems of elastic fibres that resist extension, compression, and bending. We choose the Lagrangian curvilinear coordinates (r,s) so that each fixed value of s labels a particular fibre, and we compute the total elastic forces generated by the immersed fibres as the sum of a stretching force density and a bending force density. Let $T = T(\mathbf{s})$ be the fibre tension, so that $T\,dr\,ds$ has units of force, and let $\boldsymbol{\tau} = \boldsymbol{\tau}(\mathbf{s}) = \partial\mathbf{X}/\partial s/|\partial\mathbf{X}/\partial s|$ be the unit tangent vector aligned with the fibres. We compute $\mathbf{F}$ by

$$\mathbf{F} = \frac{\partial}{\partial s}(T\boldsymbol{\tau}) + \frac{\partial^2}{\partial s^2}\left(\kappa\frac{\partial^2}{\partial s^2}\mathbf{X}\right), \tag{7}$$

in which $\kappa = EI$ is the bending stiffness coefficient, with E denoting the Young's modulus and I denoting the cross-sectional moment of inertia. For a detailed discussion of this fibre-based elasticity modelling approach, see Griffith et al. [20] and Luo et al. [22]. We remark that it is possible within the framework of the IB method to model the chordae tendinae as thin elastic rods [25,34,35], although we do not use this description herein.

2.3. Numerical methods

We use a fibre-aligned discretization of the Lagrangian equations and a uniform, staggered-grid discretization of the Eulerian equations. For further details on these spatial discretizations, see Griffith [23,24,36]. The time stepping scheme that we use is similar to that of Griffith [23]; however, in the present work we employ a second-order Adams–Bashforth scheme for the convective terms when solving the incompressible Navier–Stokes.

Briefly, let $u_{i+\frac{1}{2},j,k}, v_{i,j+\frac{1}{2},k}$, and $w_{i,j,k+\frac{1}{2}}$ denote staggered-grid approximations to the components of the Eulerian velocity field that are defined at positions $\mathbf{x}_{i+\frac{1}{2},j,k}, \mathbf{x}_{i,j+\frac{1}{2},k}$, and $\mathbf{x}_{i,j,k+\frac{1}{2}}$, respectively; let $p_{i,j,k}$ denote a cell-centered approximation to the pressure defined at positions $\mathbf{x}_{i,j,k}$; let $\mathbf{X}_{l,m}$ and $\mathbf{F}_{l,m}$ denote approximations to the position and Lagrangian elastic force density at node (l,m) of the Lagrangian curvilinear mesh; and let $\nabla_h\cdot$, ∇_h, and ∇_h^2 denote standard staggered-grid finite-difference approximations to the divergence, gradient, and Laplace operators, respectively, in which h is the Cartesian grid spacing. We denote by $\mathbf{X}^n$, $\mathbf{u}^n$, and $p^{n-\frac{1}{2}}$ approximations to the values of $\mathbf{X}$ and $\mathbf{u}$ at time t^n, and to the value of p at time $t^{n-\frac{1}{2}}$.

Given $\mathbf{X}^n$, $\mathbf{u}^n$, and $p^{n-\frac{1}{2}}$, we obtain $\mathbf{X}^{n+1}$, $\mathbf{u}^{n+1}$, and $p^{n+\frac{1}{2}}$ by first computing

$$\frac{\widetilde{\mathbf{X}}^{n+1} - \mathbf{X}^n}{\Delta t} = \mathcal{R}^n\mathbf{u}^n, \tag{8}$$

in which $\mathcal{R}^n = \mathcal{R}(\mathbf{X}^n)$ is the *velocity restriction* operator, for which $\mathbf{U}^n = (U^n, V^n, W^n) = \mathcal{R}^n\mathbf{u}^n$ is given by

$$U^n_{l,m} = \sum_{i,j,k} u^n_{i-\frac{1}{2},j,k}\ \delta_h\left(\mathbf{x}_{i-\frac{1}{2},j,k} - \mathbf{X}^n_{l,m}\right)\ h^3, \tag{9}$$

$$V^n_{l,m} = \sum_{i,j,k} v^n_{i,j-\frac{1}{2},k}\ \delta_h\left(\mathbf{x}_{i,j-\frac{1}{2},k} - \mathbf{X}^n_{l,m}\right)\ h^3, \tag{10}$$

$$W^n_{l,m} = \sum_{i,j,k} w^n_{i,j,k-\frac{1}{2}}\ \delta_h\left(\mathbf{x}_{i,j,k-\frac{1}{2}} - \mathbf{X}^n_{l,m}\right)\ h^3, \tag{11}$$

in which $\delta_h(\mathbf{x}) = \delta_h(x)\ \delta_h(y)\ \delta_h(z)$ is the four-point delta function of Peskin [33]. To obtain a time step-centered approximation to $\mathbf{X}$, we compute

$$\mathbf{X}^{n+\frac{1}{2}} = \frac{\widetilde{\mathbf{X}}^{n+1} + \mathbf{X}^n}{2}. \tag{12}$$

We next solve

$$\rho\left(\frac{\mathbf{u}^{n+1} - \mathbf{u}^n}{\Delta t} + \mathbf{A}^{n+\frac{1}{2}}\right) = -\nabla_h p^{n+\frac{1}{2}} + \mu\nabla_h^2\frac{\mathbf{u}^{n+1} + \mathbf{u}^n}{2} + \mathbf{f}^{n+\frac{1}{2}}, \tag{13}$$

$$\nabla_h\cdot\mathbf{u}^{n+1} = 0, \tag{14}$$

$$\mathbf{f}^{n+\frac{1}{2}} = \mathcal{S}\left(\mathbf{X}^{n+\frac{1}{2}}\right)\ \mathbf{F}\left(\mathbf{X}^{n+\frac{1}{2}}\right), \tag{15}$$

$$\frac{\mathbf{X}^{n+1} - \mathbf{X}^n}{\Delta t} = \mathcal{R}\left(\mathbf{X}^{n+\frac{1}{2}}\right)\ \frac{\mathbf{u}^{n+1} + \mathbf{u}^n}{2}, \tag{16}$$

for $\mathbf{X}^{n+1}$, $\mathbf{u}^{n+1}$, and $p^{n+\frac{1}{2}}$, in which $\mathbf{A}^{n+\frac{1}{2}} = \frac{3}{2}\mathbf{u}^n\cdot\nabla_h\mathbf{u}^n - \frac{1}{2}\mathbf{u}^{n-1}\cdot\nabla_h\mathbf{u}^{n-1}$ is an approximation to the nonlinear advection term computed by a version of the piecewise parabolic method (PPM) [37,38]. Here, $\mathcal{S}^n = \mathcal{S}(\mathbf{X}^n)$ is the *force prolongation* operator, for which $\mathbf{f}^{n+\frac{1}{2}} = \left(f_x^{n+\frac{1}{2}}, f_y^{n+\frac{1}{2}}, f_z^{n+\frac{1}{2}}\right) = \mathcal{S}^{n+\frac{1}{2}}\mathbf{F}^{n+\frac{1}{2}}$ is given by

$$\left(f_x^{n+\frac{1}{2}}\right)_{i+\frac{1}{2},j,k} = \sum_{l,m}(F_x)^{n+\frac{1}{2}}_{l,m}\ \delta_h\left(\mathbf{x}_{i+\frac{1}{2},j,k} - \mathbf{X}^{n+\frac{1}{2}}_{l,m}\right)\ \Delta r\ \Delta s, \tag{17}$$

$$\left(f_y^{n+\frac{1}{2}}\right)_{i,j+\frac{1}{2},k} = \sum_{l,m}(F_y)^{n+\frac{1}{2}}_{l,m}\ \delta_h(\mathbf{x}_{i,j+\frac{1}{2},k} - \mathbf{X}^{n+\frac{1}{2}}_{l,m})\ \Delta r\ \Delta s, \tag{18}$$

$$\left(f_z^{n+\frac{1}{2}}\right)_{i,j,k+\frac{1}{2}} = \sum_{l,m}(F_z)^{n+\frac{1}{2}}_{l,m}\ \delta_h(\mathbf{x}_{i,j,k+\frac{1}{2}} - \mathbf{X}^{n+\frac{1}{2}}_{l,m})\ \Delta r\ \Delta s. \tag{19}$$

Notice that by construction, $\mathcal{S}$ and $\mathcal{R}$ are adjoint operators. This property ensures that the semi-discrete scheme conserves energy during Lagrangian–Eulerian interaction [33].

This scheme must be modified during the first time step because time step-lagged values of $\mathbf{u}$ and p are not available. During the initial time step, we first solve

$$\rho\left(\frac{\tilde{\mathbf{u}}^{n+1} - \mathbf{u}^n}{\Delta t} + \mathbf{A}^n\right) = -\nabla_h\tilde{p}^{n+\frac{1}{2}} + \mu\nabla_h^2\frac{\tilde{\mathbf{u}}^{n+1} + \mathbf{u}^n}{2} + \mathbf{f}^n, \tag{20}$$

$$\nabla_h\cdot\tilde{\mathbf{u}}^{n+1} = 0, \tag{21}$$

$$\mathbf{f}^n = \mathcal{S}(\mathbf{X}^n)\ \mathbf{F}(\mathbf{X}^n), \tag{22}$$

$$\frac{\widetilde{\mathbf{X}}^{n+1} - \mathbf{X}^n}{\Delta t} = \mathcal{R}(\mathbf{X}^n)\ \mathbf{u}^n, \tag{23}$$

for $\widetilde{\mathbf{X}}^{n+1}$, $\tilde{\mathbf{u}}^{n+1}$, and $\tilde{p}^{n+\frac{1}{2}}$, where $\mathbf{A}^n = \mathbf{u}^n\cdot\nabla_h\mathbf{u}^n$. We then compute

$$\mathbf{X}^{n+\frac{1}{2}} = \frac{\widetilde{\mathbf{X}}^{n+1} + \mathbf{X}^n}{2}, \tag{24}$$

and finally solve Eqs. (13)–(16), for $\mathbf{X}^{n+1}$, $\mathbf{u}^{n+1}$, and $p^{n+\frac{1}{2}}$, except that we use $\mathbf{A}^{n+\frac{1}{2}} = \mathbf{u}^{n+\frac{1}{2}}\cdot\nabla_h\mathbf{u}^{n+\frac{1}{2}}$ with $\mathbf{u}^{n+\frac{1}{2}} = \frac{1}{2}(\tilde{\mathbf{u}}^{n+1} + \mathbf{u}^n)$.

2.4. Implementation

The simulations described herein employ the open-source IBAMR software framework (http://ibamr.googlecode.com), which provides an adaptive and distributed-memory parallel implementation of the IB method as well as infrastructure for developing FSI models that use the IB method. IBAMR leverages functionality provided by other freely available software libraries, including SAMRAI (https://computation.llnl.gov/casc/SAMRAI), PETSc (http://www.mcs.anl.gov/petsc), and *hypre* (http://www.llnl.gov/CASC/hypre).

3. Human mitral valve model

3.1. Geometry reconstruction from magnetic resonance images

A cine MR scan was performed on a healthy 28-year-old male volunteer using a 3-Tesla MRI system (Verio, Siemens, Germany). Twelve planes including the left ventricular outflow tract (LVOT)

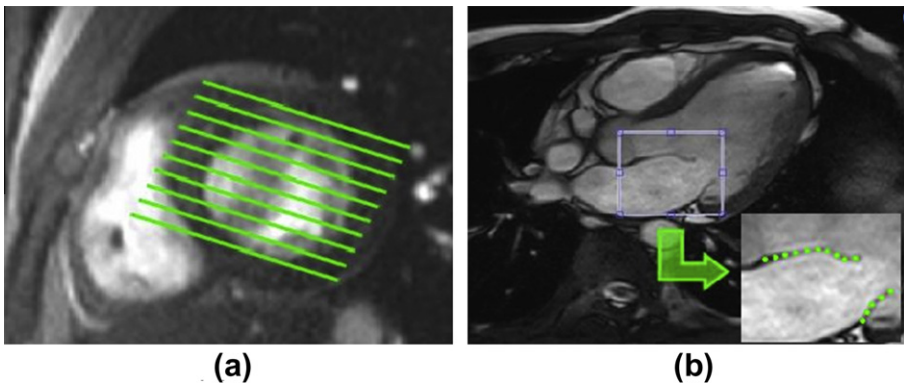

Fig. 1. Magnetic resonance images of the mitral valve. (a) Illustration of the image plane positioned to cover the whole valve. (b) Magnetic resonance image of the mitral valve showing the two leaflets and manual segmentation.

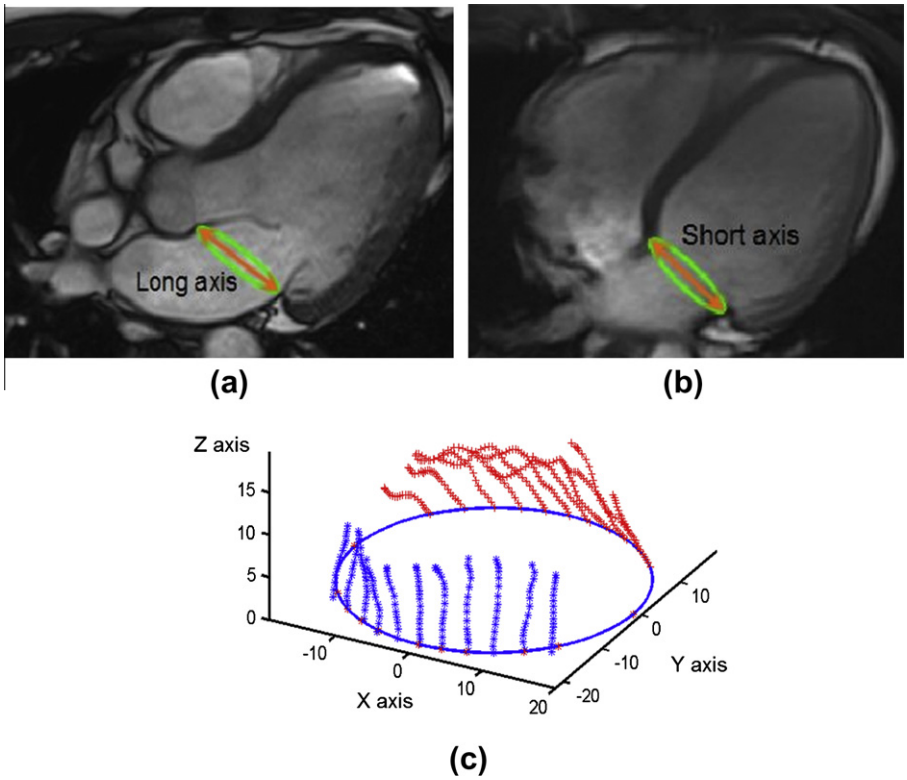

Fig. 2. Mitral valve reconstruction. (a) The long-axis measurement of mitral annulus from a LVOT slice of the valve; (b) the short-axis measurement mitral annulus from a four chamber view slice. (c) Final manual segmentation determined from images assembled along the annulus ring.

were used for MV imaging to cover the entire mitral valve, as indicated by the green[1] lines superimposed on the two-chamber view shown in Fig. 1a. The parameters for the MV MRI scan were: slice thickness: 3 mm with 0 mm gap; matrix size: 432×572; pixel size: 0.7×0.7 mm^2; frame rate: 25 per second. The MV was reconstructed at the middle of diastole when the MV is fully open.

The general steps for MV reconstruction included:

- *Annulus ring reconstruction.* The annulus ring was assumed to be an ellipse projected on a plane defined by the MV long axis and short axis shown in Fig. 2a and b.
- *Two-dimensional leaflet segmentation.* MV leaflets were manually segmented on LVOT views using two detached lines to represent the anterior and posterior leaflets. MR images for the same views at other times were also used to help identify MV boundaries.
- *Leaflet assembly.* MV leaflet segmentations from the stack of images were assembled along the reconstructed annulus rings as shown in Fig. 2c.
- *Mesh generation.* The assembled leaflet were imported into Gambit to construct the final three-dimensional mesh.

Fig. 3 shows the final mesh obtained from the Gambit mesh generation software. The leaflet surfaces are very irregular, with a concave surface in the front of the anterior leaflet and a convex face close to the annulus when facing the left ventricle.

[1] For the color version of this figure, the reader is referred to the on-line version of this article.

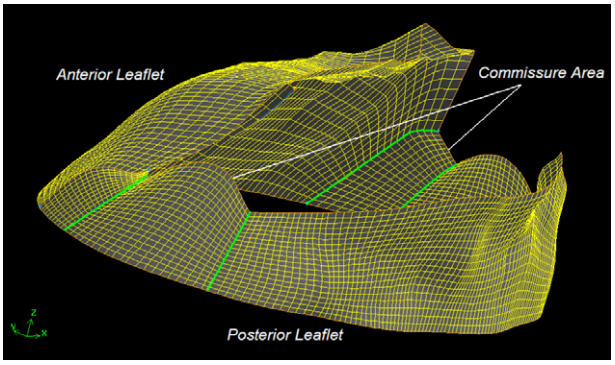

Fig. 3. Anterior and posterior leaflet meshes.

3.2. Material properties of the mitral leaflets

It has been reported that the modulus of elasticity of the MV leaflets does not vary significantly with deformation [39]. We therefore model the MV leaflets as a linear isotropic material with a Young's modulus of 0.8 MPa following previous studies on ovine MV [11,12]. We remark that Lim et al. [11] also assumed that the thickness of the leaflets is uniform. In this work, we consider two approaches to determine the thickness of the leaflets, following the measurements on a human MV [31]. One approach assumes that both leaflets have the same uniform thickness of 0.94 mm, and the other sets the thickness of the anterior leaflet to be 0.97 mm and the thickness of the posterior leaflet to be 0.92 mm [31].

3.3. Chordae tendinae

We include descriptions of only the primary chordae tendinae. In our model, these attach to the free margin of the leaflet and run through the leaflets to the annulus ring. The number and location of the chordate are based on anatomical descriptions [1,40]. Each of the chordae is attached to one of two points positioned in a plane 40 mm above the annular plane that are taken to represent the papillary muscle groups. A total of 22 evenly distributed marginal chordae are defined and between the papillary tips and leaflet free edges [41,42], with fourteen associated with the posterior leaflet and eight with the anterior leaflet; see Fig. 4. Both the mitral annulus and the papillary tips are fixed in space. The resting lengths of the chordae are set to be longer than their initial lengths to provide slack that permits the leaflets to close when subjected to a realistic systolic pressure load. Each of the chordae was assumed to have a uniform cross-sectional area of 1.15 mm^2 and an elastic modulus of 22 MPa [15].

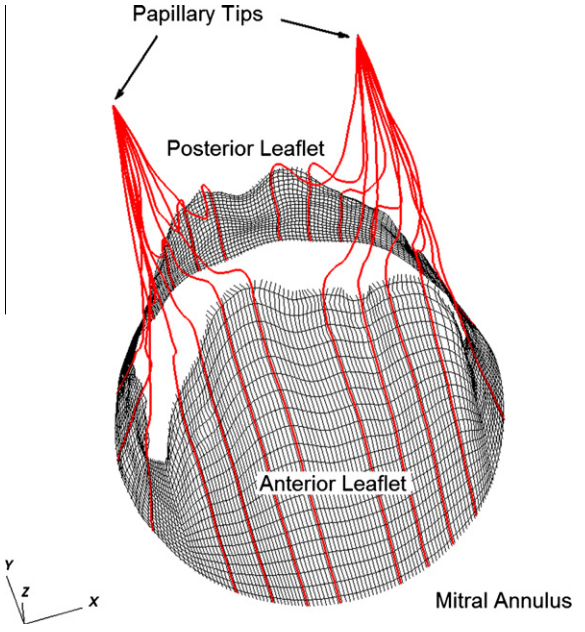

Fig. 4. A total of 22 marginal chordae shown in red are defined between the papillary tips and leaflet free edges. In our simulations, the papillary tips and the mitral annulus are fixed in place. (For interpretation of the references to colour in this figure legend, the reader is referred to the web version of this article.)

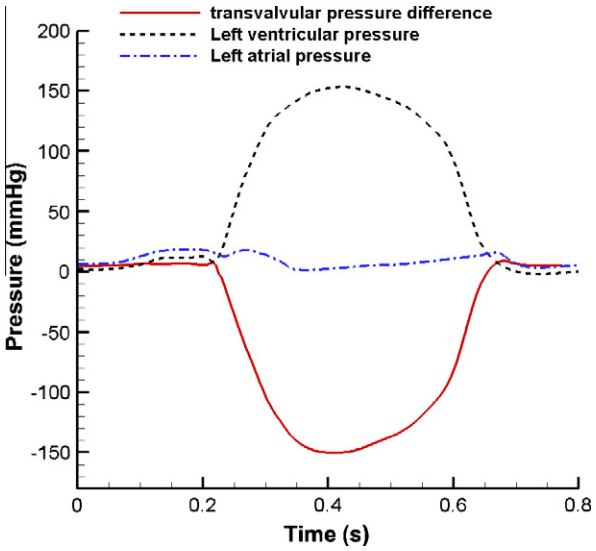

Fig. 5. Typical time courses of the left ventricular (green) and left atrial (blue) pressures. The left ventricular pressure has scaled to match the peak systolic pressure of the volunteer. The difference between these curves is the transvalvular pressure difference (dash-dot) imposed in the simulations. (For the color version of this figure, the reader is referred to the on-line version of this article.)

3.4. Driving and loading conditions

We simulate the valve dynamics for a complete cardiac cycle of 0.7 s, starting at mid-diastole, which was the time when the MR images used to construct the leaflet geometry were obtained. It is convenient to specify the pressure difference between the inlet and outlet of the tube in which the MV is mounted. Because subject-specific transvalvular pressure data were not available, we instead use a typical physiological pressure profile based on human clinical data [32]. A similar approach was adopted in previous MV models [5,43]. Here we have rescaled the data so that the peak systolic pressure is 150 mmHg, matching that of the volunteer; see Fig. 5.

4. Computational results

In the simulations, the MV annulus is fixed to a housing disc that is mounted in a semi-rigid circular tube immersed in a 16 cm × 8 cm × 8 cm fluid box, as shown in Fig. 6. A transvalvular pressure gradient is prescribed across the length of the tube, and zero-pressure boundary conditions are employed along the remainder of the domain boundary [20]. The fluid pressure and instantaneous streamlines generated by the model are shown in Fig. 7 when the valve is fully open and fully closed. The valve opens at a driving pressure of approximately 5 mmHg and is subject to a physiological downstream pressure load of 150 mmHg when fully closed.

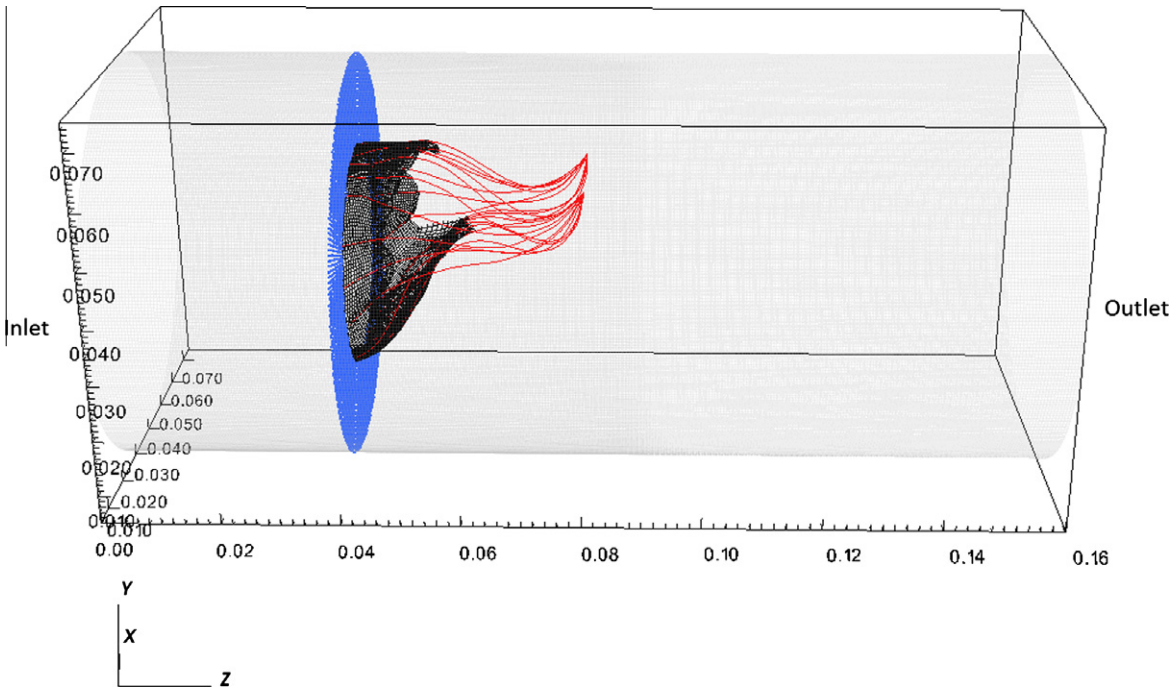

Fig. 6. The mitral annulus is fixed to a housing disc and mounted at the location of $x = 0.04$ m in a semi-rigid circular tube of length 0.16 m. The valve apparatus, including the valve leaflets and chordate tendinae, are attached to the annulus. These structures are all immersed in a 16 cm × 8 cm × 8 cm rectangular fluid box.

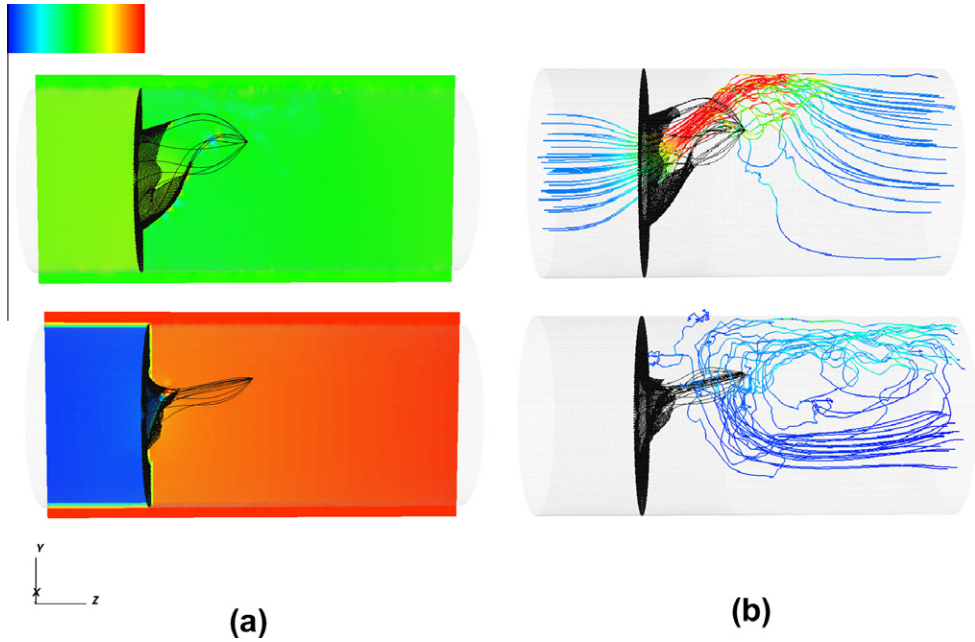

Fig. 7. (a) The fluid pressure field along the plane of $x = 0.04$ m bisecting the MV, shown when the MV is fully open (top), plotted from −200 Pa to 750 Pa, and fully closed (bottom), plotted from −20,000 Pa to −100 Pa. (b) The corresponding instantaneous streamlines of the flow, coloured by the velocity magnitude (top: from 0 to 2.3 m/s, originating from the inlet, and bottom: from 0 to 0.35 m/s, originating from the outlet). (For the color version of this figure, the reader is referred to the on-line version of this article.)

The closed and open configurations of the model valve are shown in Fig. 8 along with the corresponding MR images. Notice that in the septilateral direction, the MR image shows that the anterior leaflet surface was convex (with respect to the left ventricle) near the annulus and concave near the free edge throughout systole and diastole. Such a pattern is consistent not only with reports from animal models [44,45] but also with experimental observations in humans [46]. In our simulations, the aforementioned curvature pattern can be seen in diastole when we use either a uniform leaflet thickness or different thicknesses for the anterior and posterior leaflets, but is observed in systole only when we use different thicknesses for the leaflets. A more detailed comparison of results obtained when using these different assumptions is shown in Fig. 9, where the chordae embedded in the anterior

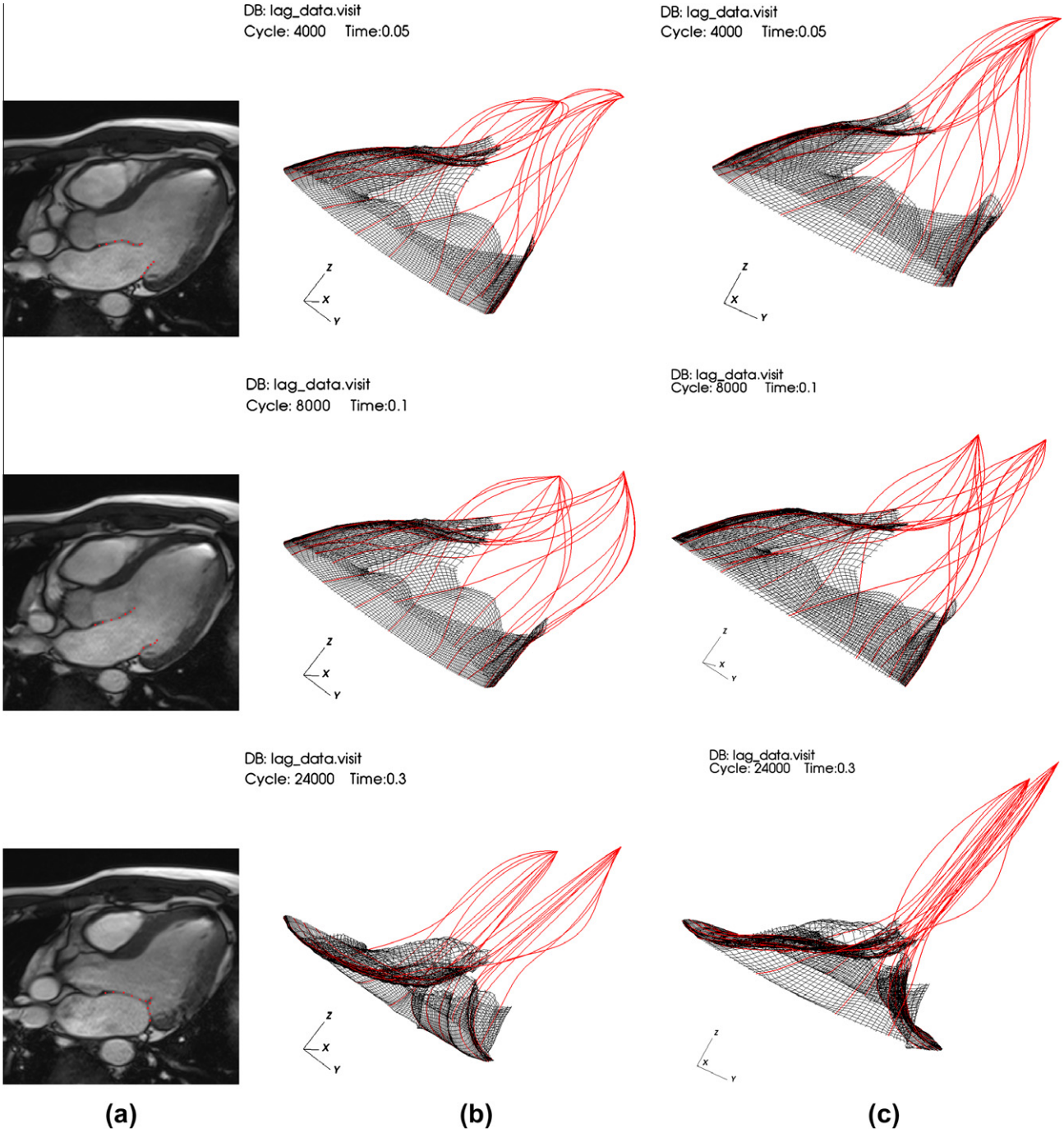

Fig. 8. Side view of the mitral valve mid-diastole (t = 0.005 s, top); fully opened (t = 0.1 s, middle); and mid-systole (t = 0.3 s, bottom). (a) MR imaging data; (b) model results obtained when using a uniform thickness for the two leaflets; and (c) model results obtained when using different thicknesses for the anterior and posterior leaflets. Notice the model that includes differences in the thickness of the leaflets is in better agreement with the clinical data.

leaflets are used to show the shape of the leaflet. These results make it clear that when we assume that both leaflets have same thickness, the stiffness of the anterior leaflet is too small and the stiffness of posterior leaflet is too large.

The flow rate through the valve is shown in Fig. 10. These data further support the finding that the model that uses different thicknesses for the anterior and posterior leaflets yields a closer agreement to the measurements. It is also clear that this model produces smaller flow oscillations during closure. We remark that the second peak in the measured flow rate is due to the left atrim contraction. This additional ventricular loading is not considered in our simulation.

5. Discussion and conclusions

In this study, we described the development of an anatomically realistic human MV model based on in vivo MR imaging data, and we presented fully three-dimensional FSI simulations using this model under physiological, dynamic transvalvular pressure loads. An initial validation of the model is provided by comparing the computed opening shape and flow rates to clinical measurements from the volunteer who provided the anatomical data used to construct the model.

Recent in vivo studies have highlighted the importance of anterior leaflet shape in MV closure [43]. The anterior leaflet was

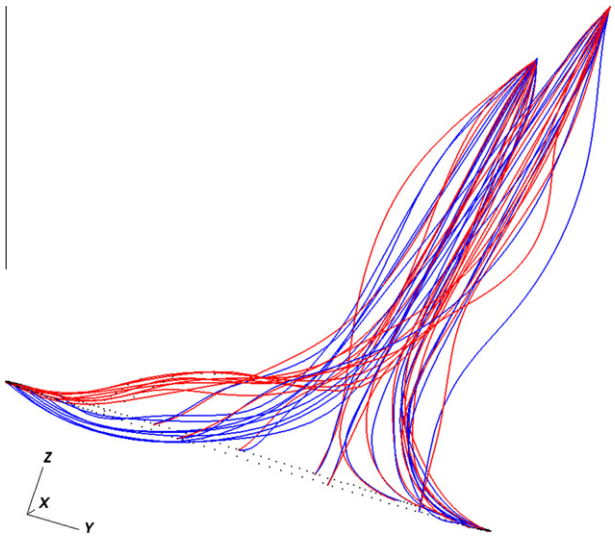

Fig. 9. The shape of the MV in the closed configuration as shown by fibres embedded in the leaflets for the cases in which different thicknesses are used for the leaflets (red-solid) and the case in which the same thickness is used for both leaflets (blue-dotted). This view shows that the anterior leaflet is convex near the annulus and concave near the free edge only when we use different thicknesses for the two leaflets. (For interpretation of the references to colour in this figure legend, the reader is referred to the web version of this article.)

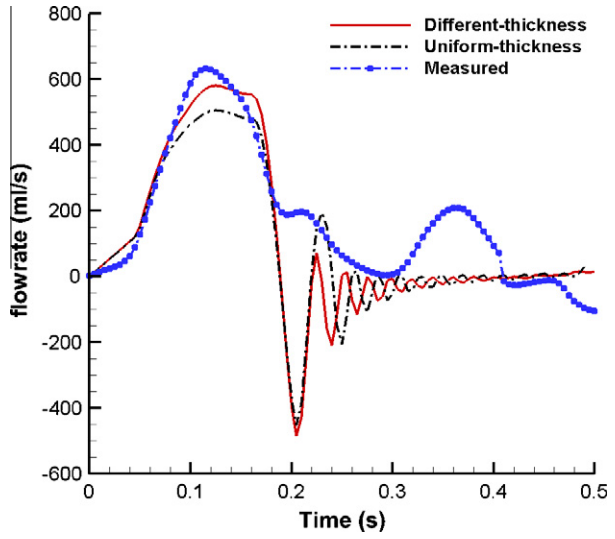

Fig. 10. Flow rates produced by the mitral valve models along with clinical flow data obtained from phase contrast cine MRI. Agreement between the model results and the experimental data is best when the model includes different thicknesses for the anterior and posterior leaflets.

observed clinically to be convex (with respect to the LV) near the annulus, and concave close to the free edges in the septilateral direction [44–46]. This shape is observed in our simulations, but only when we assign physiological thicknesses [31] to the two leaflets. These results suggest that differences in the thicknesses of the leaflets play an important role in maintaining the physiological curvature of the MV. Accounting for the difference in the thicknesses of the leaflets also reduces the effective resistance of the valve and increases the flow rate during diastole, yielding better agreement between the computed flow rate and the clinical data. The flow rate is proportional to the opening orifice of the MV [47], which is one of the key aspects in MV performance. These results highlight that these thickness differences also have an important functional role.

We note, however, that there remains some discrepancy between the computed and measured flow rates, particularly as the flow is decelerating. Specifically, much larger oscillations are seen in the computed flow rates when compared to the clinical measurements. We expect that this is primarily because of the lack of realistic compliance in the pressure loading provided by our model [22]. We also assumed the uniform thickness within each leaflet; however, in the real valve, there is a small spatial variation in the thickness [31]. Each of these limitations in the model could have additional impacts in the shape changes, but they have not been taken into account in this work.

It was convenient to develop the initial geometrical model of the MV leaflets from a fully open configuration. We also kept the mitral annulus and papillary muscle tips fixed in space. Doing so required us to set the resting lengths of the chordae to be longer than their initial lengths to allow the valve to close when subjected to a physiological pressure load. A more realistic approach, not considered here, would be to incorporate a description of the kinematics of the papillary tips, as done previously [19,21].

Another limitation of this work is the relatively simple isotropic material model that is use to describe the MV leaflets. The real valve is anisotropic, with collagen fibres distributed along the circumferential direction. We are presently developing an extension of this model that accounts for this material anisotropy within the context of the nonlinear hyperelastic MV constitutive model of May-Newman and Yin [48]. To do so, we plan to replace the present fibre-based elasticity model by a nonlinear finite element method using a recent extension of the IB method [49].

Acknowledgments

X.S.M. was sponsored by a China Scholarship Council studentship and fee waiver funding from the University of Glasgow. B.E.G. acknowledges research support from the American Heart Association (AHA award 10SDG4320049) and the National Science Foundation (NSF awards DMS-1016554 and OCI-1047734). We are also grateful for funding from the UK EPSRC (EP/I1029990), the British Heart Foundation, Medical Research Scotland, the Royal Society of Edinburgh, and the Royal Academy of Engineering.

References

[1] Muresian H. The clinical anatomy of the mitral valve. Clin Anat 2009;22(1):85–98.
[2] Gabriel V, Kamp O, Visser CA. Three-dimensional echocardiography in mitral valve disease. Euro J Echocardio 2005;6(6):443–54.
[3] Lau KD, Diaz V, Scambler P, Burriesci G. Mitral valve dynamics in structural and fluid-structure interaction models. Med Eng Phys 2010;32(9):1057–64.
[4] Prot V, Skallerud B. An improved transverse isotropic hyperelastic material model for simulation of mitral valve response. J Biomech 2006;39. S618.
[5] Prot V, Haaverstad R, Skallerud B. Finite element analysis of the mitral apparatus: annulus shape effect and chordal force distribution. Biomech Model Mechanobiol 2009;8(1):43–55.
[6] Prot V, Skallerud B. Nonlinear solid finite element analysis of mitral valves with heterogeneous leaflet layers. Comput Mech 2009;43(3):353–68.
[7] Prot V, Skallerud B, Sommer G, Holzapfel GA. On modelling and analysis of healthy and pathological human mitral valves: two case studies. J Mech Behav Biomed Mater 2010;3(2):167–77.
[8] Skallerud B, Prot V, Nordrum IS. Modeling active muscle contraction in mitral valve leaflets during systole: a first approach. Biomech Model Mechanobiol 2011;10(1):1–16.
[9] Votta E, Maisano F, Alfieri O, Montevecchi FM, Redaelli A. Finite element models of newly shaped prosthetic rings for the correction of functional mitral regurgitation. J Biomech 2006;39. S293–S293.
[10] Votta E, Maisano F, Bolling SF, Alfieri O, Montevecchi FM, Redaelli A. The geoform disease-specific annuloplasty system: a finite element study. Ann Thor Surg 2007;84(1):92–101.
[11] Lim KH, Yeo JH, Duran CM. Three-dimensional asymmetrical modeling of the mitral valve: a finite element study with dynamic boundaries. J Heart Valve Dis 2005;14(3):386–92.
[12] Kunzelman KS, Cochran RP, Chuong C, Ring WS, Verrier ED, Eberhart RD. Finite element analysis of the mitral valve. J Heart Valve Dis 1993;2(3):326–40.

[13] Einstein DR, Reinhall P, Nicosia M, Cochran RP, Kunzelman K. Dynamic finite element implementation of nonlinear, anisotropic hyperelastic biological membranes. Comput Meth Biomech Biomed Eng 2003;6(1):33–44.
[14] Einstein DR, Kunzelman KS, Reinhall PG, Nicosia MA, Cochran RP. Non-linear fluid-coupled computational model of the mitral valve. J Heart Valve Dis 2005;14(3):376–85.
[15] Kunzelman KS, Reimink MS, Cochran RP. Annular dilatation increases stress in the mitral valve and delays coaptation: a finite element computer model. Cardiovasc Surg 1997;5(4):427–34.
[16] Kunzelman KS, Reimink MS, Cochran RP. Flexible versus rigid ring annuloplasty for mitral valve annular dilatation: a finite element model. J Heart Valve Dis 1998;7(1):108–16.
[17] Reimink MS, Kunzelman KS, Cochran RP. The effect of chordal replacement suture length on function and stresses in repaired mitral valves: a finite element study. J Heart Valve Dis 1996;5(4):365–75.
[18] Watton PN, Luo XY, Wang X, Bernacca GM, Molloy P, Wheatley DJ. Dynamic modelling of prosthetic chorded mitral valves using the immersed boundary method. J Biomech 2007;40(3):613–26.
[19] Watton PN, Luo XY, Yin M, Bernacca GM, Wheatley DJ. Effect of ventricle motion on the dynamic behaviour of chorded mitral valves. J Fluids Struct 2008;24(1):58–74.
[20] Griffith BE, Luo X, McQueen DM, CS P. Simulating the fluid dynamics of natural and prosthetic heart valves using the immersed boundary method. Int J Appl Mech 2009;1(1):137–77.
[21] Yin M, Luo XY, Wang TJ, Watton PN. Effects of flow vortex on a chorded mitral valve in the left ventricle. Int J Numer Meth Biomed Eng 2010;26(3-4):381–404.
[22] Luo XY, Griffith BE, Ma XS, Yin M, Wang TJ, Liang CL, et al. Effect of bending rigidity in a dynamic model of a polyurethane prosthetic mitral valve. Biomech Model Mechanobiol 2012;11(6):815–27.
[23] Griffith BE. Immersed boundary model of aortic heart valve dynamics with physiological driving and loading conditions. Int J Numer Meth Biomed Eng 2012;28(3):317–45.
[24] Griffith BE. On the volume conservation of the immersed boundary method. Commun Comput Phys 2012;12:401–32.
[25] Griffith BE, Lim S. Simulating an elastic ring with bend and twist by an adaptive generalized immersed boundary method. Commun Comput Phys 2012;12:433–61.
[26] Lai MC, Peskin CS. An immersed boundary method with formal second-order accuracy and reduced numerical viscosity. J Comput Phys 2000;160(2):705–19.
[27] Griffith BE, Peskin CS. On the order of accuracy of the immersed boundary method: higher order convergence rates for sufficiently smooth problems. J Comput Phys 2005;208(1):75–105.
[28] Clark RE, Butterworth GA. Characterization of the mechanics of human ortic and mitral valve leaflets. Surg Forum 1971;22:134–6.
[29] Ghista DN, Rao AP. Structural mechanics of the mitral valve: stresses sustained by the valve; non-traumatic determination of the stiffness of the in vivo valve. J Biomech 1972;5(3):295–6.
[30] Clark RE. Stress–strain characteristics of fresh and frozen human aortic and mitral leaflets and chordae tendineae. implications for clinical use. J Thoracic Cardiovasc Surg 1973;66(2):202–8.
[31] McDonald PC, Wilson JE, McNeill S, Gao M, Spinelli JJ, Rosenberg F, et al. The challenge of defining normality for human mitral and aortic valves: geometrical and compositional analysis. Cardiovasc Pathol 2002;11(4):193–209.
[32] Levick JR. An introduction to cardiovascular physiology 5E. Hodder Education; 2012.
[33] Peskin CS. The immersed boundary method. Acta Numer 2002;11:479–517.
[34] Lim S, Ferent A, Wang XS, Peskin CS. Dynamics of a closed rod with twist and bend in fluid. SIAM J Scient Comput 2008;31:273–302.
[35] Lim S. Dynamics of an open elastic rod with intrinsic curvature and twist in a viscous fluid. Phys Fluids 2010;22(2):024104. p. 11.
[36] Griffith BE. An accurate and efficient method for the incompressible Navier–Stokes equations using the projection method as a preconditioner. J Comput Phys 2009;228(20):7565–95.
[37] Colella P, Woodward PR. The piecewise parabolic method (ppm) for gas-dynamical simulations. J Comput Phys 1984;54(1):174–201.
[38] Rider WJ, Greenough JA, Kamm JR. Accurate monotonicity- and extrema-preserving methods through adaptive nonlinear hybridizations. J Comput Phys 2007;225(2):1827–48.
[39] Miller GE, Hunter JF, Lively WM. A note on mitral valve mechanics: a pre-stressed leaflet concept. J Biomech 1981;14(5):373–5.
[40] Sakai T, Okita Y, Ueda Y, Tahata T, Ogino H, Matsuyama K, et al. Distance between mitral anulus and papillary muscles: anatomic study in normal human hearts. J Thoracic Cardiovasc Surg 1999;118(4):636–41.
[41] Hammer PE, Vasilyev NV, Perrin DP, Del Nido PJ, Howe RD. Fast image-based model of mitral valve closure for surgical planning. In: MIDAS journal, computational biomechanics for medicine (MICCAI 2008 Workshop); 2008. p. 15–26.
[42] Votta E, Caiani E, Veronesi F, Soncini M, Montevecchi FM, Redaelli A, et al. Philos Trans R Soc A: Mathe Phys Eng Sci 2008;366(1879):3411–34.
[43] Stevanella M, Maffessanti F, Conti CA, Votta E, Arnoldi A, Lombardi M, et al. Mitral valve patient-specific finite element modeling from cardiac mri: application to an annuloplasty procedure. Cardiovasc Eng Technol 2011;2(2):66–76.
[44] Kvitting JPE, Bothe W, Göktepe S, Rausch MK, Swanson JC, Kuhl E, et al. Anterior mitral leaflet curvature during the cardiac cycle in the normal ovine heart. Circulation 2010;122(17):1683–9.
[45] Karlsson MO, Glasson JR, Bolger AF, Daughters GT, Komeda M, Foppiano LE, et al. Mitral valve opening in the ovine heart. Am J Physiol-Heart Circul Physiol 1998;274(2):H552–63.
[46] Ryan R, Abbara S, Colen RR, Arnous S, Quinn M, Cury RC, et al. Cardiac valve disease: spectrum of findings on cardiac 64-mdct. Am J Roentgenol 2008;190(5):W294–303.
[47] Gorlin R, Gorlin SG. Hydraulic formula for calculation of the area of the stenotic mitral valve, other cardiac valves, and central circulatory shunts. Am Heart J 1951;41(1):1–29.
[48] May-Newman K, Yin FC. Biaxial mechanical behavior of excised porcine mitral valve leaflets. Am J Physiol-Heart Circul Physiol 1995;269(4):H1319–27.
[49] Griffith BE, Luo X. Hybrid finite difference/finite element version of the immersed boundary method, submitted for publication.